

Tuned ionic mobility by Ultrafast-laser pulses in Black Silicon

Christelle Inès K. Mebou,^{1,2} Martin E. Garcia,^{1,2} and Tobias Zier^{3,*}

¹*Theoretische Physik, Universität Kassel, Heinrich-Plett-Str. 40, 34132 Kassel, Germany*

²*Center for Interdisciplinary Nanostructure Science and Technology (CINSaT), Heinrich-Plett-Str. 40, 34132 Kassel, Germany*

³*Department of Physics, University of California Merced, Merced, CA 95343*

Highly non-equilibrium conditions in femtosecond-laser excited solids cause a variety of ultrafast phenomena that are not accessible by thermal conditions, like sub-picosecond solid-to-liquid or solid-to-solid phase transitions. In recent years the microscopic pathways of various laser-induced crystal rearrangements could be identified and led to novel applications and/or improvements in optoelectronics, photonics, and nanotechnology. However, it remains unclear what effect a femtosecond-laser excitation has on ionic impurities within an altered crystal environment, in particular on the atomic mobility. Here, we performed ab-initio molecular dynamics (AIMD) simulations on laser-excited black silicon, a promising material for high-efficient solar cells, using the Code for Highly excited Valence Electron Systems (CHIVES). By computing time-dependent Bragg peak intensities for doping densities of 0.16% and 2.31% we could identify the overall weakening of the crystal environment with increasing impurity density. The analysis of Si-S bond angles and lengths after different excitation densities, as well as computing interatomic forces allowed to identify a change in ion mobility with increasing impurity density and excitation strength. Our results indicate the importance of impurity concentrations for ionic mobility in laser-excited black silicon and could give significant insight for semiconductor device optimization and materials science advancement.

I. INTRODUCTION

Intense femtosecond-laser excitations induce harsh conditions in solids, mostly because the extremely high peak power is mainly transferred to the electronic system, whereas the ions remain nearly unaffected. As a consequence, the electronic occupation is changed dramatically, directly influencing the interatomic bonding¹⁻⁴. This allows microscopic ionic pathways that are non-accessible under thermal conditions, which are the foundation of a variety of ultrafast laser-induced phenomena, like solid-to-liquid phase transitions⁵⁻⁹, solid-to-solid phase transitions¹⁰⁻¹⁵, coherent ionic motions¹⁶⁻²², and even liquid-to-liquid phase transitions²³. Intensive investigations using experimental time-resolved techniques, like X-ray²⁴⁻²⁷ or electron diffraction²⁸⁻³² as well as theoretical efforts to simulate those effects using AIMD^{33,34}, Tight-binding approaches³⁵⁻³⁸, classical MD³⁹⁻⁴², time-dependent DFT⁴³⁻⁴⁷ or other approaches shed light on a variety of underlying microscopic mechanisms and led to fascinating applications. In particular, the progress in the field of material processing using ultrafast lasers is impressive^{48,49}. It's now possible to produce structures of the size of critical transport properties⁵⁰ by modifying material surfaces⁵¹, drill nano-precision holes⁵², create uniform distributed nano-ripples⁵³, or produce nanodroplets⁵⁴ and material cones^{55,56}.

Besides changing and manipulating crystalline structures by ultrafast-laser light it is possible to alter material properties by doping^{57,58}. Using experimental techniques, like ion bombardment⁵⁹, crystal growth⁶⁰, sputtering⁶¹, and thermal diffusion⁶², it is possible to insert different ionic species into a host material. For example, it is an intriguing approach⁶³⁻⁶⁵ to introduce dopants to silicon in order to manipulate its essential characteristics like the electronic band gap or optical

properties. However, some methodical challenges appear, like dopant diffusivity⁶⁶ or dopant activity while maintaining the crystalline structure in the host material⁶⁷.

Laser-assisted ion migration is combining the benefits of both approaches, in which crystal properties can be manipulated twice, 1) by the laser excitation and the ensuing crystal changes and 2) by the diffusion of impurities into the crystal. Furthermore, the laser-excitation could produce voids or other crystal changes that allow the ions to migrate the crystal in the first place. In such a way, ions of a gaseous environment could diffuse into the initial crystalline material under femtosecond-laser excitation. Among these dopant materials Sulfur (S) has drawn a lot of attention⁶⁸⁻⁷⁰, because of its promising improvements for photodiodes, photodetectors, solar cells and antibacterial materials⁷¹⁻⁸⁷. By using silicon as crystal host material in a sulfur environment intense femtosecond-laser excitations could produce under certain conditions black silicon^{75,88,89}. The crystal of black silicon is characterized by the formation of nm to μm sized needles at the surface due to the laser excitation, which incorporate sulfur atoms from the environment. In this configuration, the absorption is increased over the range from 250 to 2500 nm⁹⁰ while the reflection is reduced to a few percent^{90,91}. Additionally, experiments show that the photocurrent could be increased by up to 60%⁹². We like to note, that black silicon can also be produced by other techniques, like dry or wet etching^{88,93,94}, but the use of femtosecond-lasers can reduce the number of fabrication steps⁹⁵, which in general reduces potential influences and/or sources of error. However, the mechanisms behind migration, diffusion and distribution mechanisms of defects and/or impurities, here sulfur ions, during and after an ultrafast-laser excitation is unknown.

We performed ab-initio MD simulations of doped silicon with an impurity density of 0.46% and 2.32% and

compared it to our reference system of pristine silicon. Note, that we don't simulate the needle/cone formation or the capturing of sulfur atoms within, rather we studied the mobility change of sulfur dopants in a silicon host crystal. All computations were done using the Code for Highly Excited Valence Electron Systems (CHIVES). The rest of the paper is structured as followed: Sec. II summarizes the main simulation details, characteristics of CHIVES, and definitions used for computed quantities. After that, in Sec. III we will present our MD simulation results by analyzing, e.g., our obtained time-dependent Bragg peak intensities, bond angles and bond lengths of Si-S bonds and interatomic forces on specific atoms. This is followed by a discussion of effects contributing to a mobility change and the possibility to tune it in Sec. IV.

II. SIMULATION DETAILS

In order to study the mobility change of impurities in laser-excited crystals we compared the structural responses of three different supercells with 0%, 0.46%, and 2.32% impurity density. We used the data of the supercell with zero impurities as a reference for the silicon atom mobility and refer to it in this work as pristine silicon. The supercell itself was constructed by repeating the cubic unit cell, which contains 8 silicon atoms, $3 \times 3 \times 3$ in x , y , and z -direction, respectively. Hence, the total number of atoms in the supercell sums up to 216. In the case of 0.46% impurity density we replaced randomly one silicon atom of the pristine silicon cell by a sulfur atom. For the highest dopant density five randomly chosen silicon atoms were interchanged with sulfur. In order to avoid artificial forces or effects we relaxed the doped supercells. For each of the three data sets we initialized 10 independent runs near 315 K using the approach described in¹⁸. We like to note, that in each run five different silicon atoms were interchanged. Moreover, we checked that no sulfur clusters were formed, meaning we avoided nearest neighbor atoms to be replaced. The lattice parameter for the cubic unit cell is $a = 10.2021a_0 = 0.5398747278$ nm. The initialized supercells created in this way, were used as input for the MD simulations performed in CHIVES.

A. Specifics used in CHIVES

CHIVES is a Mermin DFT code that can compute electronic properties for nonzero electronic temperatures^{18,96,97}. All computations presented here used the local density approximation (LDA) for the exchange-correlation functional. The cut-off energy for the Hartree, exchange, and correlation potentials was set to 1330 eV. Tightly bonded core electrons are described by norm-conserving pseudopotentials⁹⁸, whereas the valence electrons are accounted for by atom-centered Gaussian basis sets. Silicon atoms are described using

the following exponents, which were already published in¹⁸ $\alpha_1 = 1.77509a_0^{-2}$ (s and p orbitals) $\alpha_2 = 0.55380a_0^{-2}$ (s , p and d orbitals) $\alpha_3 = 0.16270a_0^{-2}$ (s and p orbitals). For the sulfur dopants we established a basis set with 17 states and the exponents $\alpha_1 = 1.17769a_0^{-2}$ (s and p orbitals) $\alpha_2 = 0.40348a_0^{-2}$ (s , p and d orbitals) $\alpha_3 = 0.12989a_0^{-2}$ (s and p orbitals). The perturbation of the electronic system by a femtosecond-laser excitation is modelled by an instant increase of the electronic temperature. That corresponds to a δ -pulse excitation above the materials band gap and the approximation that the electrons thermalize fast, namely within the first time step. Consistent to that electronic temperature the electrons are distributed over the Kohn-Sham states using the corresponding Fermi-Dirac distribution. Interatomic forces computed by CHIVES are then incorporated into a Velocity-Verlet scheme to connect electrons and ions and to enable MD simulations. Here, we used a timestep of $\Delta t = 1$ fs. Highly parallelized subroutines allow to perform propitious calculations, in particular on non-symmetric and/or disordered systems.

B. Bragg peak intensities

With the aim of gaining information about the structural deformations and variations of black silicon after femtosecond-laser irradiation we computed the time-evolution of Bragg peak intensities, which could directly be compared to data obtained by time-resolved diffraction experiments using X-rays or electrons. In general, the intensity I can be expressed in terms of the time-dependent structure factor F :

$$I_{\mathbf{q}}(t) = |F_{\mathbf{q}}(t)|^2 \quad (1)$$

with $\mathbf{q} = \frac{2\pi}{a}(h, k, l)$ as the scattering vector and h , k , l the Miller indices defining the scattering plane. Given that our crystal contains two different types of atoms, Si and S, the structure factor itself can be expressed as the total of the contributions made by each species:

$$F_{\mathbf{q}}(t) = \sum_{j=1}^{N_1} f_{j,1} e^{i\mathbf{q} \cdot r_{j,1}(t)} + \sum_{k=1}^{N_2} f_{k,2} e^{i\mathbf{q} \cdot r_{k,2}(t)} \quad (2)$$

with N_1 and N_2 the total number of atoms of each type in the supercell, $f_{j,1} = 14$ and $f_{k,2} = 16$ the scattering factors of the j -th atom of type 1 (Si) and the k -th atom of type 2 (S)⁹⁹, $r_{j,1}$ and $r_{k,2}$ the position vectors of the j -th atom of type 1 and the k -th atom of type 2 in the unit cell, respectively. We note, that the intensity in the presented form is dependent on the number of atoms in the supercell. With the intention of getting rid of this dependency we normalized $I_{\mathbf{q}}(t = 0)$ to 1. Note, that the intensities shown in Fig. 1 are averaged over our ten independent runs. The width is indicating the errors in the averages.

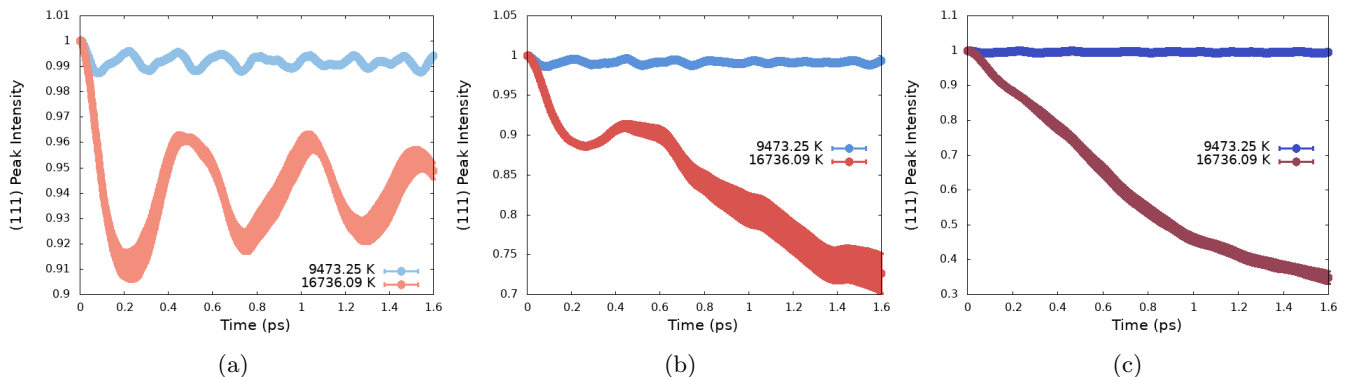


FIG. 1: Normalized time-evolution of the (111) Bragg intensity after femtosecond-laser excitations that induce electronic temperatures $T_1 = 9473.25$ K (blue-ish solid curves) and $T_2 = 16736.09$ K (red-ish solid curves), respectively. (a) Laser-induced coherent oscillations in pristine silicon. (b) For a dopant density of 0.46% the crystal destabilizes for the higher excitation with T_2 . (c) This trend is even accelerated for the dopant density of 2.31%. The crystal remains stable for all densities and an excitation to T_1 . Note, the different scale in intensity between the densities. The width of the lines indicate the error in the average.

C. Si-S bond lengths and angles

Another insight of the ionic dynamics after the laser-excitation is provided by the evolution of the Si-S bond length. We obtained an approximation of the bond length b by averaging the distance to first neighbor silicon atoms from each sulfur dopant using

$$b = \frac{1}{N_S N_{nn}} \sum_{i=1}^{N_S} \sum_{j=1}^{N_{nn}} |\mathbf{r}_i^S - \mathbf{r}_j^{Si}|, \quad (3)$$

with N_S is the number of dopants, N_{nn} is the number of nearest neighbors, \mathbf{r}_S is the position of a sulfur dopant, and \mathbf{r}_j^{Si} is the position the dopants nearest Si neighbors. Again, we averaged this quantity over our ten independent runs.

Moreover, we computed the Si-S-Si bond angle θ and its time-evolution by using

$$\theta = \frac{1}{6N_S} \sum_{i=1}^{N_S} \sum_{i,j>i}^6 \arccos \left(\frac{\mathbf{r}_i^{Si-S} \cdot \mathbf{r}_j^{Si-S}}{|\mathbf{r}_i^{Si-S}| |\mathbf{r}_j^{Si-S}|} \right), \quad (4)$$

with $\mathbf{r}_{i,j}^{Si-S} = \mathbf{r}_{i,j}^{Si} - \mathbf{r}^S$.

III. AIMD SIMULATION RESULTS

Coming back to our initial question "how is the mobility of dopants changed within a host crystal after an ultrashort optical excitation?" we analyzed the above described simulations. In the following, we show and compare the results for two different excitation strength, realized by two electronic temperatures, namely $T_1 = 30$ mHa ≈ 9473.25 K and $T_2 = 53$ mHa ≈ 16736.09 K. T_1

corresponds to a moderate excitation for which no irreversible structural changes are induced¹⁰⁰. T_2 is close to but below the threshold of laser-induced disordering processes that will definitely destroy the crystal symmetry.

In a first attempt, we analyzed the evolution of Bragg peak intensities after the excitation (see Fig. 1). In the left panel of Fig. 1(a) the results for pristine silicon are plotted. Without any impurities present in the crystalline system the intensity only decreases by around 9%, even for the higher temperature. This indicates that no irreversible or disordering processes are induced within the simulation timescale. For both electronic temperatures oscillations in the Bragg intensities are visible. Those can be attributed to thermal phonon squeezing¹⁸. Surprisingly, an impurity density of 0.46%, here a single Si atom was interchanged by S, has already a drastic impact on the overall system's response to optical excitations (see Fig. 1 (b)). Whereas the moderate excitation to T_1 seems comparable to pristine silicon, the case for T_2 came out completely different. Within the simulation time the intensity drops by roughly 30%, indicating disordering processes in which atoms move far away from their equilibrium positions and destroying the crystal symmetries. Interestingly, the first stages, up to 400 fs, show a similar behavior as pristine silicon, namely an oscillatory behavior (see Fig. 1 (b), red curve). However, the oscillation does not continue and the intensity drops. Thereafter the atoms follow other pathways by overcoming laser-changed local bonding, which accelerates them away from their initial local minimum. In addition we like to point out that within the first 400 fs the width of the curve in Fig. 1 (b) is relatively small, which means that basically all atoms in all independent runs behave at least very similar if not the same. After this period the width increases, indicating different atomic behavior between the runs, which is typical at transition thresholds. In summary, the interchange of a single silicon atom with

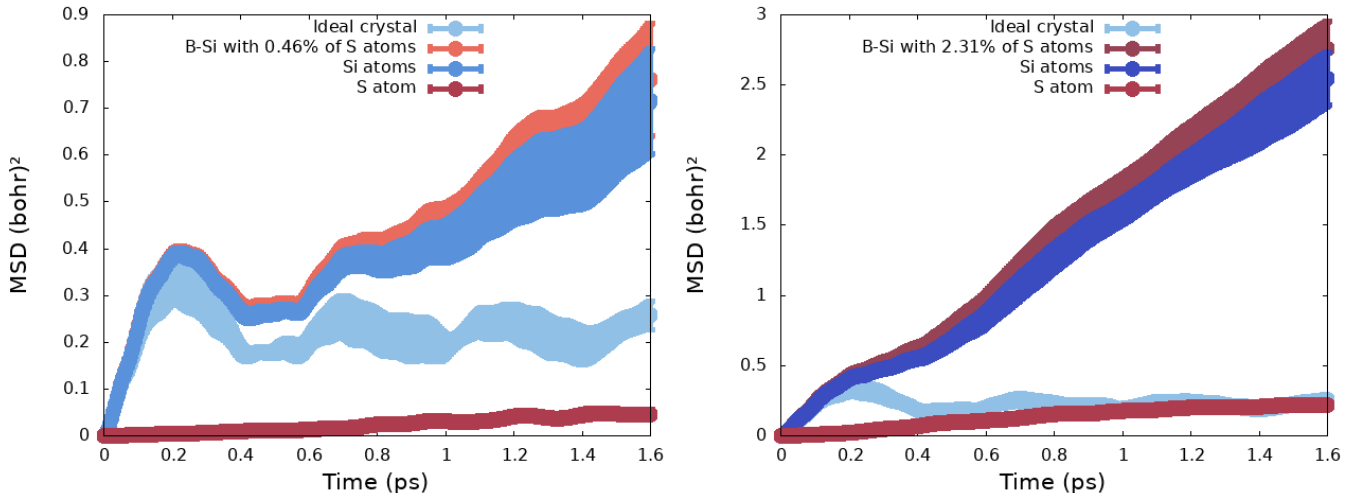


FIG. 2: Averaged MSD for an electronic temperature $T_2 = 16736.09$ K as a function of time and a dopant density of 0.46% (left panel, light red) and 2.31% (right panel, red-brown), respectively. The values for pristine silicon is given as a reference (light blue) in both figures. The decomposition into the silicon host crystal (blue) and the sulfur impurities (red, bottom curve).

sulfur reduced the threshold for irreversible structural changes and increased the ionic mobility within the structure. This trend is even aggravated after increasing the dopant density to 2.31% (see Fig. 1 (c)). The intensity drops by almost 70% within the simulation time. Moreover, there are no longer any signs of oscillations visible, the transient maximum is only slightly visible at around 200 fs. The dopant density has therefore a direct influence on the crystal's response after femtosecond-laser excitation and the ion mobility. Note, that the results for an additional Bragg direction can be found in Appendix. However, this analysis of the Bragg intensity is an average over the whole crystal, which makes it impossible to decide which amount can be attributed to the movement of sulfur atoms and what comes from the silicon host material. Therefore, we computed the mean-square atomic displacement (MSD) by

$$MSD(t, 0) = \frac{1}{N_1 + N_2} \sum_{i=1}^{N_1} |r_i(t) - r_i(0)|^2 + \frac{1}{N_1 + N_2} \sum_{j=1}^{N_2} |r_j(t) - r_j(0)|^2. \quad (5)$$

Here, N_1 and N_2 are the numbers of atoms for each type, $r_{i,j}(t)$ is the position vector of atom i,j at time t , $r_{i,j}(0)$ the initial position vector of atom i,j at time $t = 0$. Figure 2 shows the results for $T_2 = 16736.09$ K for both dopant densities 0.46% (left panel) and 2.31% (right panel). Compared to pristine silicon (light blue), the MSD of 0.46% shows an increasing behavior (light red in Fig. 2) to around 0.75 bohr². This is in accordance to the intensity drop in the (111) Bragg peak we discussed before. Furthermore, Fig. 2 shows the decomposition of

the total MSD into the contributions from the silicon host crystal (blue in Fig. 2) and the sulfur impurities (dark red Fig. 2). We observed that most is contributed to the total MSD by the silicon host crystal. However, we recognized a monotonic increased contribution by the sulfur atoms. A similar behavior, but on a different scale could be observed in the case of the higher dopant density. In this case the sulfur atoms reach the average displacement of pristine silicon within the simulation time. Surprisingly, this result indicates an enormous mobility increase in the host material and not for the impurities. This means, in the case of mobility that the host crystal benefits of the impurities, or in other words that the impurities destabilize the crystalline structure without moving exorbitantly themselves.

In order to investigate the changes occurring in the vicinity of the impurities we changed to quantities that are sensitive to microscopic changes, like the bond length of impurity atoms to nearest neighbors. Since our results indicated a mostly similar crystal response, except the scale, we will from here on only show results for the high dopant density of 2.31%. The results for the lower density can be found in Appendix. Figure 3 shows the bond length evolution after the excitation. For the lower excitation to T_1 the bond length stays close to its initial value with a small decreasing trend at the end of the simulation, which indicates that the microscopic arrangement around the impurity is remaining diamond-like and the atoms don't move that far. For the higher excitation (red curve in Fig. 3) the bond length increased about 10% within our simulation. This is also observable by the shift to larger values of the nearest neighbor distance in the pair-correlation function (see Appendix) at this electronic temperature. Interestingly, the bond length change is not a monotonic increase but rather showing

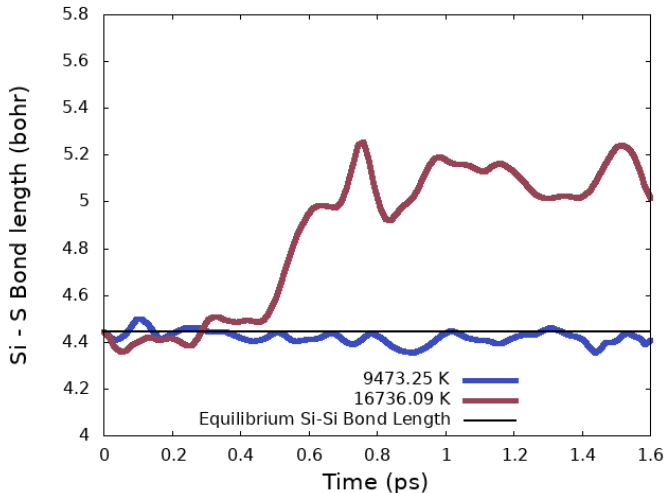


FIG. 3: Bond length evolution of impurities to neighboring atoms as a function of time after the excitation for a dopant density of 2.31%.

some dips. It starts with a shortening of the interatomic bond length within the first 200 fs, which could be attributed to the induced pressure by the excitation. After that the bond length increases by almost 10% before showing a big dip at around 800 fs. At around this time the MSD starts to increase linearly with time, indicating that the system behaves diffusive. Therefore, scattering events become more probable that could change the direction of motion of the impurities or the surrounding ions, which could also push the impurity back towards its initial position. Nevertheless, on average the distance of impurities to its neighbors increase.

We see a similar behavior in the time-evolution of the bond angle in the vicinity of sulfur atoms (See Fig. 4). The results for an excitation to T_1 (red line in Fig. 4) shows an oscillation around the the ideal angle of 109.5° , which means that the diamond-like structure is maintained. The interatomic bonding remains mostly intact, the ions oscillate around their initial positions without destroying so much the crystal's symmetry. In the case of a higher excitation, here T_2 (Fig. 4, blue curve), we can also see some oscillations of the bond angle, in particular in the first 400 fs. After that period it drops to around 80° , a change of almost 30%, indicating a dramatic change on the microscopic environment around the sulfur dopants. Again, we see a rebound to the initial angle at around 800 fs, a possible recovery of the tetrahedral, diamond-like structure. Then we see a recurring drop in the bond angle with a subsequent slow increase.

In order to shed light on this behavior we analyzed the interatomic forces acting on the sulfur atoms as a function of displacement. CHIVES computes the interatomic forces for every timestep of the simulation on the fly, meaning that the potential energy surface (PES) that describes the interatomic bonding is updated every timestep to the new positions of the ions. It's gradient

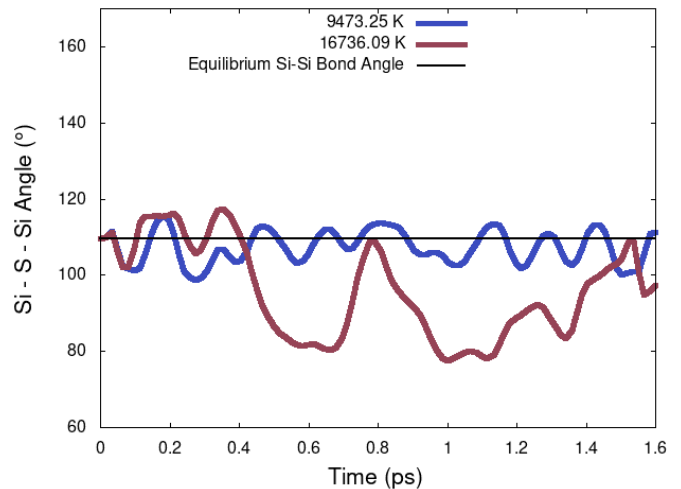


FIG. 4: Time-evolution of the averaged bond angle in the vicinity of an impurity.

gives the interatomic forces. The averaged absolute value of the force is shown in Fig. 5 (left panel). In the first 600 fs, indicated by the color code, we see a constant increase in the atomic displacement, while the forces during this time, with exception of the initial acceleration during the first 150 fs, do not show large variations. In other words, the impurities are accelerated after the excitation due the laser-changed bonding in the crystal, but move relatively free through the crystal. After about 700 fs the ions reach a root-mean-square displacement between 2.0 and 2.5 bohr and remain in this range for another 700 fs. Several direction changes and peaks in the force magnitude indicate a larger number of scattering events during this time of the simulation. The 3D plot of the forces (see Fig. 5, right panel) as a function of the time after the laser-excitation and the root-mean-square displacement unravel the knot structure between 2.0 and 2.5 bohr in the 2D plot. By comparing those results to the ones with lower sulfur density (see Appendix) at the same level of excitation we recognized that in the latter case the sulfur ions on average move farther away from their initial position. In addition, the scattering that causes substantial direction changes takes place at much later times. As a result, the ionic mobility of the dopants depend strongly on the laser-excitation but also on the dopant density. A higher dopant density will have a larger impact on the stability of the crystal. As a consequence the ions of the host material will start to move more easily, which will cause ion scattering much earlier than at lower dopant densities. In other words, a higher dopant density will improve the host materials mobility, which will decrease the dopant mobility due to much more often occurring scattering events.

Our observation that the impurities have a strong impact on the host crystal and its ion mobility can also be seen in the diffusion coefficient. It is a measure of the rate at which particles move within a material as a result

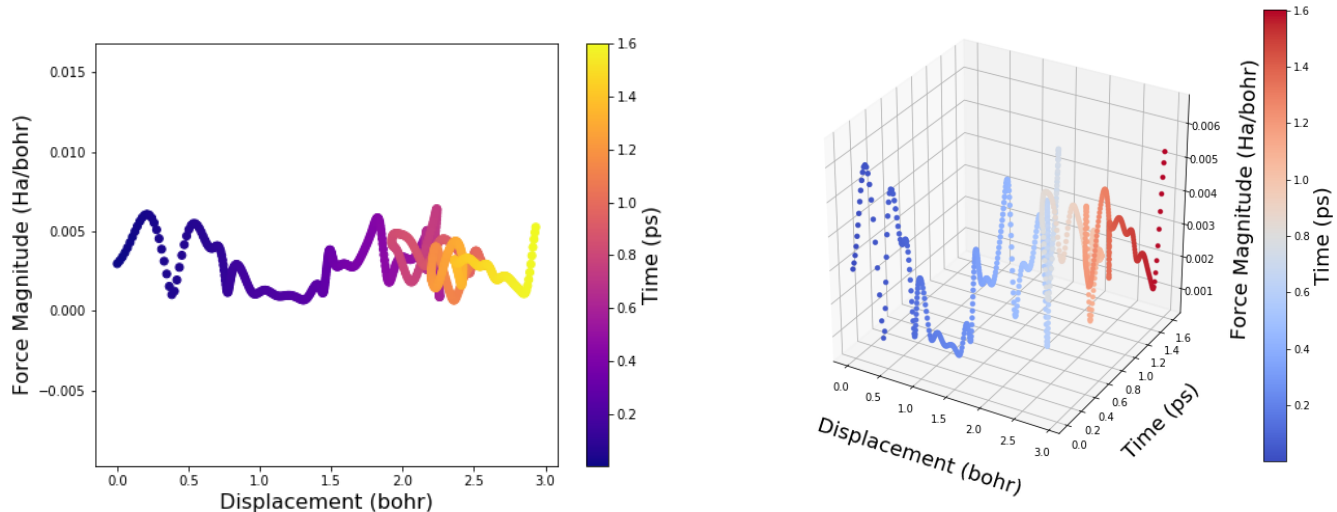


FIG. 5: (left panel) Interatomic forces acting on sulfur atoms as a function of their root-mean-square atomic displacement. The color indicates the time after the excitation, when the corresponding displacement is reached. (right panel) 3D plot of the interatomic forces as a function of the displacement and time after the excitation. In this way the knot-like structure was unraveled.

of temperature fluctuations or outside disturbances. Figure 6 shows the electronic temperature dependence of the diffusion coefficient for pristine silicon (light blue), silicon with one sulfur impurity per supercell (0.46%, blue), and silicon with sulfur density of 2.31% (dark blue). The diffusion coefficient D was computed from MSD (See Eq. 5) by using the Einstein relation:

$$D = \frac{1}{6} \lim_{t \rightarrow \infty} \left(\frac{d}{dt} MSD(t) \right) \quad (6)$$

In agreement with previous observation in this work we see at each electronic temperatures that the diffusion coefficient is largest for the highest dopant density (2.31%), showing the highest mobility but also the most scattering events. The inset in Fig. 6 shows the difference between pristine silicon and silicon with the highest dopant density in this work. We observe that for increasing electronic temperature the difference becomes larger before it reaches a plateau or even decrease again. The reason for that is, at some excitation level the crystalline structure destabilized predominantly due to the extremely laser-changed bonding properties, which become much larger than the locally changed properties due to impurities.

IV. EFFECTS ON THE IMPURITY MOBILITY

In summary, our present work on sulfur-doped silicon has shed light on the dynamic behaviour after a femtosecond-laser excitation on the microscopic level. In more detail, by performing ab initio molecular dynamics,

we studied the motion and mobility of sulfur atoms in a silicon host crystal. Furthermore, we analyzed the ionic mobility in dependence of the dopant density and the laser-excitation strength. Our results show, that at the same level of excitation, here electronic temperature, the increase of dopants has a direct influence on the threshold after which irreversible structural changes are induced by the excitation. The time-evolution of Bragg peak intensities indicates that this threshold is reduced with increasing number of dopants. The weakening of the crystal's bonding can be explained by the additional change of the local bonding by the dopant. Interestingly, this has a larger effect on the ions of the host material than on the dopants. The contributions of the host crystal and the dopants to the total MSD show that on average each silicon ion moved twice as far away than in the pristine comparison system (Fig. 2, left panel) or even more, whereas the dopant contribution is relatively small. Analyzing the dopant vicinity by calculating bond angles and lengths, we found that the diamond like structure is nearly preserved for moderate excitation but can undergo drastic changes at higher excitation strengths. For example can the bond angle change from the equilibrium value of 109.5° to below 80° . However, our results indicate several rebounds, at least in the bond angle, which implies that the dopant also stabilizes its crystal vicinity. The bond length in this case changes to larger values as also seen in the shift of the nearest neighbor peak in the pair-correlation function. This causes more scattering events and a slow down of ions in general. In the case of high dopant density and electronic temperature the ions are more likely to get stuck at earlier times and

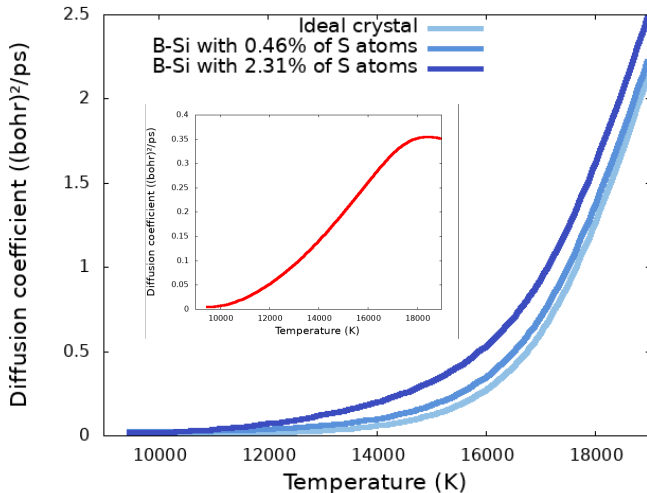


FIG. 6: Diffusion coefficient as a function of electronic temperature for three different dopant densities 0, 0.46%, and 2.31%, respectively. The inset shows the difference between the diffusion coefficients of our supercell with 2.31% of S atoms and the pristine silicon.

smaller displacements due to ion-ion scattering that at lower densities or pristine crystals. Generating black silicon by altering the crystalline structure by femtosecond-laser pulses and the migration of sulfur atoms into the material from the environment can now be tuned by two parameters, the excitation strength and the dopant density. Our results show, that the dopant mobility can be tuned over a relatively large region but going to the extremes is not beneficial. In future works, we like to investigate the dopant mobility by additionally including vacancies in the system. Furthermore, we are interested in following the microscopic pathways of the migration process. In silicon all lattice sites are defined by symmetry, therefore, it would be of interest to study the tuning of ion mobility in materials with more degrees of freedom.

ACKNOWLEDGMENTS

Calculations for this research were conducted on the Lichtenberg high performance computer of the TU Darmstadt and the IT Service center (ITS) University of Kassel. C.I.K.M. was supported by the Doctoral scholarship from the University of Kassel. T.Z. was supported by the Deutsche Forschungsgemeinschaft (DFG) through the projects GA 465/18-1 and ZI 1858/1-1. M.E.G. acknowledges support from the DFG through project GA 465/27-1.

Appendix A: Additional data

In order to have a concise description of the main points of our work and improve the readability we moved some data used in this work to the Appendix. The interested reader can find in the following the pair-correlation function, additional Bragg peak intensities and the interatomic forces for the low density dopant supercell.

1. Pair-correlation-function

In a highly symmetric crystal accumulations of atoms are found at particular distances, which are characteristic for the given material. The pair-correlation function (pcf) is a quantity that scans the crystal and counts all atoms at a certain distance. It is possible to obtain the pcf by

$$g(r) = \sum_{i,j} \frac{G(r - r_{ij})}{2\pi r^2 N}, \quad (\text{A1})$$

with G a Gaussian with full width at half maximum of 0.1 \AA and r_{ij} the distance between atom i and j . The Gaussian is used to smoothen the results of our finite supercell. Figure 7 (left panel) shows the results of the pcf for a dopant density of 0.46%. As a reference we plotted the ground state distribution at $t = 0 \text{ fs}$ (blue curve). The three other curves correspond to different electronic temperatures, namely $T_1 = 30 \text{ mHa} \approx 9473.25 \text{ K}$ (orange), $T_2 = 53 \text{ mHa} \approx 16736.09 \text{ K}$ (green), and additionally $T_3 = 60 \text{ mHa} \approx 18946.52 \text{ K}$ (red). All pcf shown here are computed for ionic configuration corresponding to the last timestep in our simulation. $t = 1.6 \text{ ps}$. For T_1 only small changes in the magnitude can be recognized even for large interatomic distances. Note, that the positions of the peaks remain the same, indicating the existing of the diamond-like crystalline structure with all symmetries. Increasing the electronic temperature to T_2 introduces noticeable changes to the distribution. First, the long range order got washed out by merging peaks. Second, increasing peaks between the main peaks of the ground state. Third, the nearest neighbor peak at around 4.4 bohr shifts slightly to larger distances. Increasing the electronic temperature (T_3) even more causes the total loss of crystalline symmetry. No distinguished peaks are recognizable, the function transitions to the form of a liquid system. In the case of higher dopant density (see Fig. 7, right panel) we see a similar behavior for T_1 . The pcf in the case of T_2 shows also a loss of long range order but a more pronounced movement of the nearest neighbor peak to longer distances. This is in agreement with our finding of the increased bond length after laser-excitation.

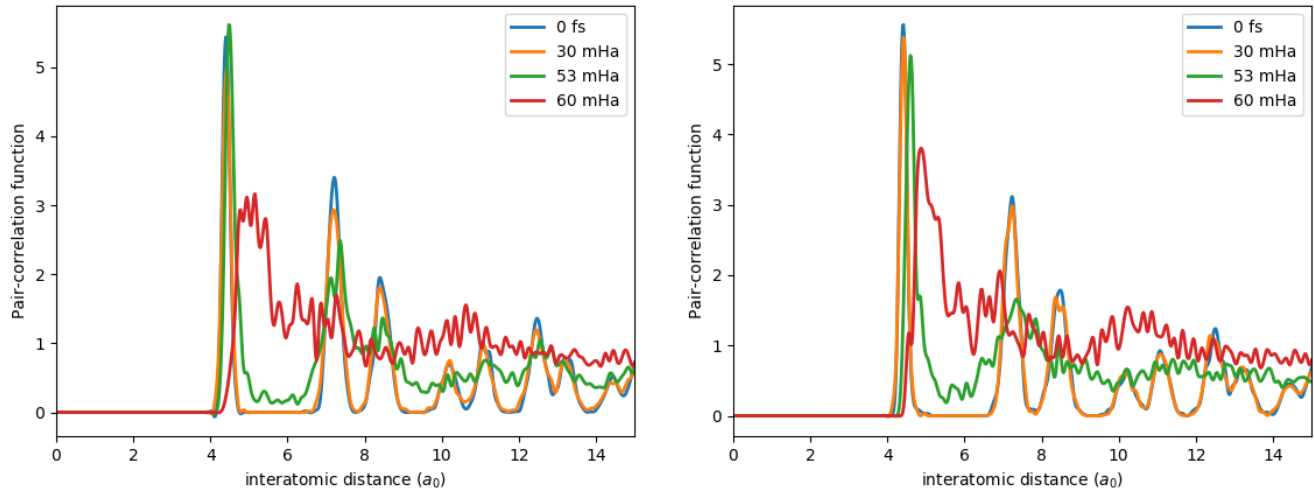


FIG. 7: Pair-correlation function for a dopant density of 0.46% (left panel) and 2.31% (right panel), respectively, for different electronic temperatures. As a reference we plotted the ground state distribution at $t = 0$ fs (blue). All other distributions are computed for the ionic distribution at the end of our simulation.

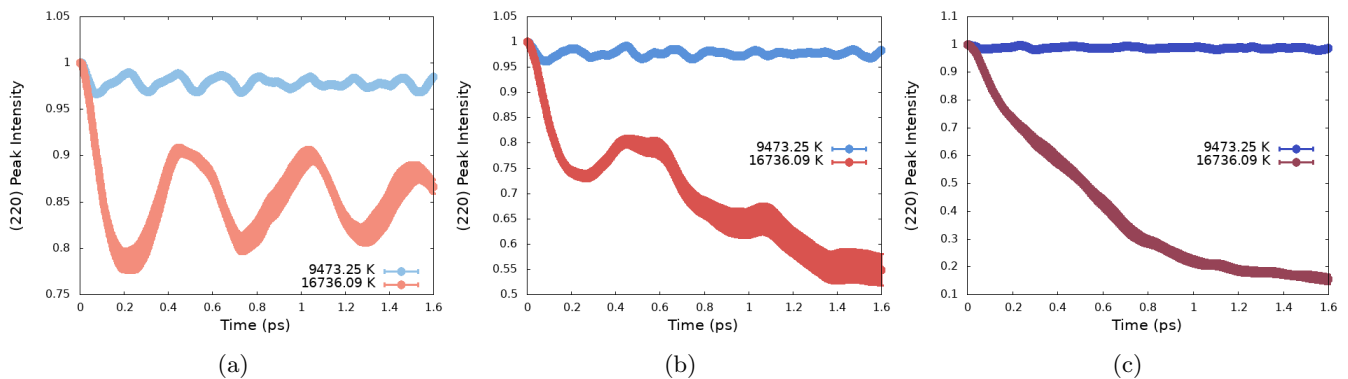


FIG. 8: Normalized time-evolution of the (220) Bragg intensity after femtosecond-laser excitations that induce electronic temperatures $T_1 = 9473.25$ K (blue-ish solid curves) and $T_2 = 16736.09$ K (red-ish solid curves), respectively. (a) Laser-induced coherent oscillations in pristine silicon. (b) For a dopant density of 0.46% the crystal destabilizes for the higher excitation with T_2 . (c) This trend is even accelerated for the dopant density of 2.31%. The crystal remains stable for all densities and an excitation to T_1 . Note, the different scale in intensity between the densities. The width of the lines indicate the error in the average.

2. (220) Bragg peak intensity

In addition to the time-evolution of the (111) Bragg peak intensities we added the intensities for the (220) peak here. Figure 8 shows the intensities for the (220) direction at the same conditions mentioned in the main text. In fact, the same behavior can be observed only the scale of the effect is slightly larger.

3. Interatomic forces on impurities

For completeness we show here the interatomic forces data for the low dopant density of 0.46% and electronic temperature T_1 (Fig. 9, (a) and (b)) and T_2 (Fig. 9, (c) and (d)). In addition, we show the results for the high dopant density 2.31% and electronic temperature T_1 (Fig. 9, (e) and (f)).

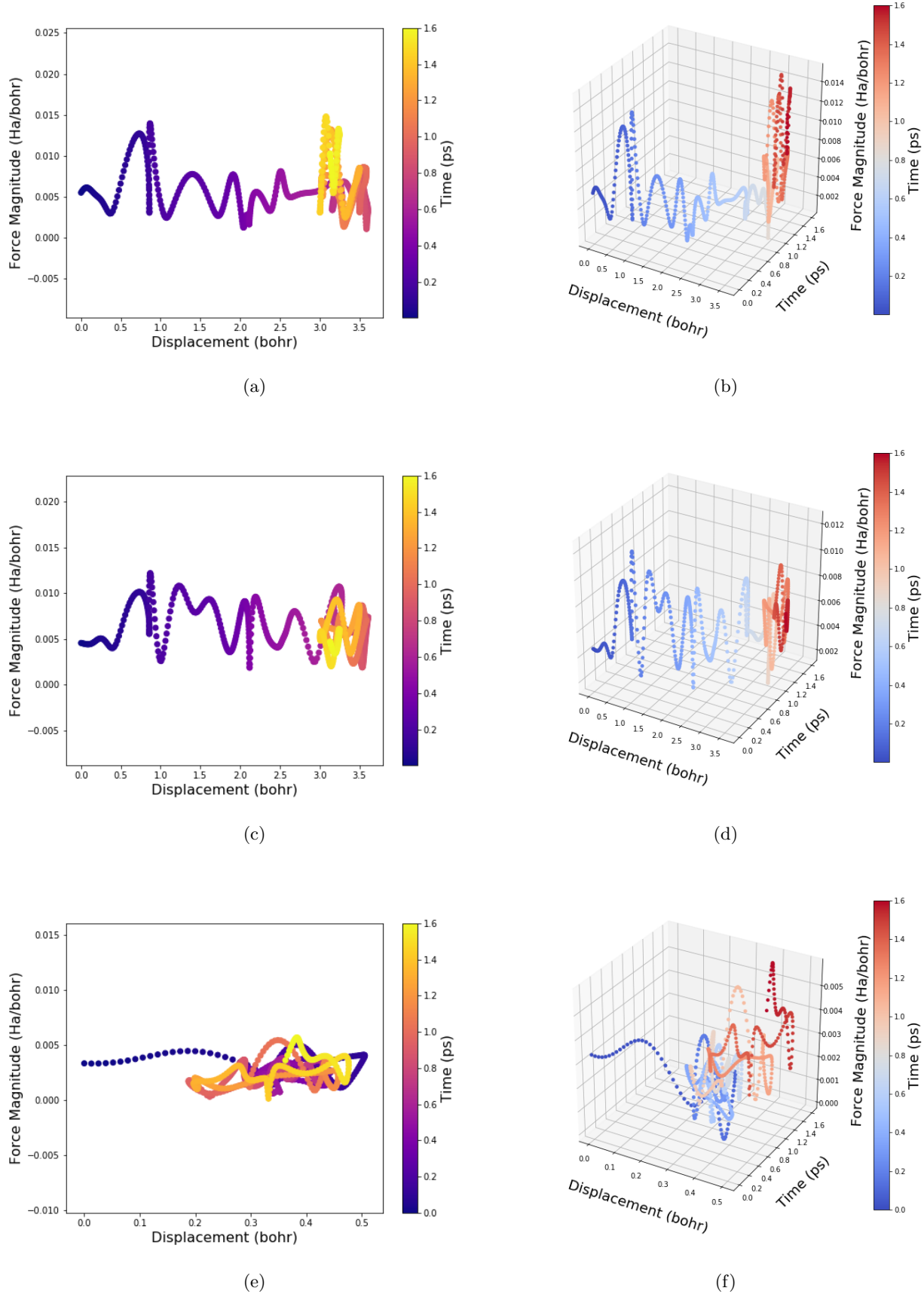


FIG. 9: Forces acting on Sulfur atoms as a function of atoms displacements (left panels) and as a function of atomic displacement and time (right panels) for different electronic temperatures and dopant densities.

- * tzier2@ucmerced.edu
- ¹ J. S. Graves and R. E. Allen, Phys. Rev. B **58**, 13627 (1998).
 - ² B. Rethfeld, K. Sokolowski-Tinten, D. Von Der Linde, and S. I. Anisimov, Applied Physics A **79**, 767 (2004).
 - ³ L. Jiang, A.-D. Wang, B. Li, T.-H. Cui, and Y.-F. Lu, Light: Science & Applications **7**, 17134 (2018).
 - ⁴ E. Gamaly, *Femtosecond Laser-Matter Interactions: Solid-Plasma-Solid Transformations at the Extreme Energy Density* (Jenny Stanford Publishing, 2022).
 - ⁵ K. Sokolowski-Tinten, J. Bialkowski, and D. von der Linde, Physical review B **51**, 14186 (1995).
 - ⁶ M. Kandyła, T. Shih, and E. Mazur, Phys. Rev. B **75**, 214107 (2007).
 - ⁷ S. Dhanjal, S. V. Popov, I. R. Shatwell, Y. P. Svirko, N. I. Zheludev, and V. E. Gusev, Opt. Lett. **22**, 1879 (1997).
 - ⁸ V. Recoules, J. Cl  rouin, G. Z  rah, P. M. Anglade, and S. Mazevet, Phys. Rev. Lett. **96**, 055503 (2006).
 - ⁹  . U. J. Bengtsson, J. C. Ekstr  m, X. Wang, A. Jurgaitis, V.-T. Pham, D. Kroon, and J. Larsson, Struct. Dyn. **7**, 054303 (2020).
 - ¹⁰ I. L. Shumay and U. H  fer, Phys. Rev. B **53**, 15878 (1996).
 - ¹¹ J. Gaudin, O. Peyrusse, J. Chalupsk  y, M. Toufarov  , L. Vy  n, V. H  jkov  , R. Sobierajski, T. Burian, S. Dastjani-Farahani, A. Graf, M. Amati, L. Gregoratti, S. P. Hau-Riege, G. Hoffmann, L. Juha, J. Krzywinski, R. A. London, S. Moeller, H. Sinn, S. Schorb, M. St  rmer, T. Tschentscher, V. Vorl  cek, H. Vu, J. Bozek, and C. Bostedt, Phys. Rev. B **86**, 024103 (2012).
 - ¹² Y. Giret, S. L. Daraszewicz, D. M. Duffy, A. L. Shluger, and K. Tanimura, Phys. Rev. B **90**, 094103 (2014).
 - ¹³ M. Makita, I. Vartiainen, I. Mohacsi, C. Caleman, A. Diaz, H. O. J  nsson, P. Jurani  , N. Medvedev, A. Meents, A. Mozzanica, N. L. Opara, C. Padeste, V. Panneels, V. Saxena, M. Sikorski, S. Song, L. Vera, P. R. Willmott, P. Beaud, C. J. Milne, B. Ziaja-Motyka, and C. David, Scientific Reports **9**, 602 (2019).
 - ¹⁴ F. Tavella, H. H  ppner, V. Tkachenko, N. Medvedev, F. Capotondi, T. Golz, Y. Kai, M. Manfredda, E. Pedersoli, M. J. Prandolini, N. Stojanovic, T. Tanikawa, U. Teubner, S. Toleikis, and B. Ziaja, High Energy Density Physics **24**, 22 (2017).
 - ¹⁵ C. A. Thomann, A. Wittrock, A. Wittig, N. F. Lopes Dias, D. Stangier, W. Tillmann, and J. Debus, APL Materials **11**, 031106 (2023).
 - ¹⁶ Y. M. Chang, L. Xu, and H. W. K. Tom, Phys. Rev. Lett. **78**, 4649 (1997).
 - ¹⁷ S. Fomichev, S. Popruzhenko, D. Zaretsky, and W. Becker, Journal of Physics B: Atomic, Molecular and Optical Physics **36**, 3817 (2003).
 - ¹⁸ E. S. Zijlstra, A. Kalitsov, T. Zier, and M. E. Garcia, Physical Review X **3**, 011005 (2013).
 - ¹⁹ T. Kimata, K. Yoda, H. Matsumoto, H. Tanabe, F. Minami, Y. Kayanuma, and K. G. Nakamura, Phys. Rev. B **101**, 174301 (2020).
 - ²⁰ R. Shayduk, J. Hallmann, A. Rodriguez-Fernandez, M. Scholz, W. Lu, U. B  senberg, J. M  ller, A. Zozulya, M. Jiang, U. Wegner, R.-C. Secareanu, G. Palmer, M. Emons, M. Lederer, S. Volkov, I. Lindfors-Vrejoiu, D. Schick, M. Herzog, M. Bargheer, and A. Madsen, Applied Physics Letters **120**, 202203 (2022).
 - ²¹ B. Ma, R.-T. Liu, X.-D. Zhang, Q. Wang, and H.-L. Zhang, The Journal of Physical Chemistry Letters **13**, 3072 (2022), pMID: 35353521, 10.1021/acs.jpcclett.2c00583.
 - ²² Y. Luo, A. Martin-Jimenez, M. Pisarra, F. Martin, M. Garg, and K. Kern, Nature Communications **14**, 3484 (2023).
 - ²³ P. Zalden, F. Quirin, M. Schumacher, J. Siegel, S. Wei, A. Koc, M. Nicoul, M. Trigo, P. Andreasson, H. Enquist, M. J. Shu, T. Pardini, M. Chollet, D. Zhu, H. Lemke, I. Ronneberger, J. Larsson, A. M. Lindenberg, H. E. Fischer, S. Hau-Riege, D. A. Reis, R. Mazzarello, M. Wuttig, and K. Sokolowski-Tinten, Science **364**, 1062 (2019).
 - ²⁴ V. V. Temnov, University of Duisburg-Essen: Duisburg, Germany (2004).
 - ²⁵ H. Khan, A. S. Yerramilli, A. D'Oliveira, T. L. Alford, D. C. Boffito, and G. S. Patience, The Canadian Journal of Chemical Engineering **98**, 1255 (2020).
 - ²⁶ S. Pandey, R. Bean, T. Sato, I. Poudyal, J. Bielecki, J. Cruz Villarreal, O. Yefanov, V. Mariani, T. A. White, C. Kupitz, M. Hunter, M. H. Abdellatif, S. Bajt, V. Bondar, A. Echelmeier, D. Doppler, M. Emons, M. Frank, R. Fromme, Y. Gevorkov, G. Giovanetti, M. Jiang, D. Kim, Y. Kim, H. Kirkwood, A. Klimovskaia, J. Knoska, F. H. M. Koua, R. Letrun, S. Lisova, L. Maia, V. Mazalova, D. Meza, T. Michelat, A. Ourmazd, G. Palmer, M. Ramilli, R. Schubert, P. Schwander, A. Silenzi, J. Sztuk-Dambietz, A. Tolstikova, H. N. Chapman, A. Ros, A. Barty, P. Fromme, A. P. Mancuso, and M. Schmidt, Nature Methods **17**, 73 (2020).
 - ²⁷ X. Ou, X. Qin, B. Huang, J. Zan, Q. Wu, Z. Hong, L. Xie, H. Bian, Z. Yi, X. Chen, Y. Wu, X. Song, J. Li, Q. Chen, H. Yang, and X. Liu, Nature **590**, 410 (2021).
 - ²⁸ C. Lin and J. Xu, Physical Chemistry Chemical Physics **14**, 13133 (2012).
 - ²⁹ M. Harb, R. Ernstorfer, C. T. Hebeisen, G. Sciaini, W. Peng, T. Dartigalongue, M. A. Eriksson, M. G. Lagally, S. G. Kruglik, and R. J. D. Miller, Phys. Rev. Lett. **100**, 155504 (2008).
 - ³⁰ J. Yang, X. Zhu, J. P. F. Nunes, J. K. Yu, R. M. Parrish, T. J. A. Wolf, M. Centurion, M. G  hr, R. Li, Y. Liu, B. Moore, M. Niebuhr, S. Park, X. Shen, S. Weathersby, T. Weinacht, T. J. Martinez, and X. Wang, Science **368**, 885 (2020).
 - ³¹ M. Hada, Y. Nishina, and T. Kato, Accounts of Chemical Research **54**, 731 (2021), pMID: 33319986.
 - ³² Z. Huang, E. S. Grape, J. Li, A. K. Inge, and X. Zou, Coordination Chemistry Reviews **427**, 213583 (2021).
 - ³³ T. Zier, E. S. Zijlstra, A. Kalitsov, I. Theodonis, and M. E. Garcia, Structural Dynamics **2** (2015).
 - ³⁴ P. L. Silvestrelli, A. Alavi, M. Parrinello, and D. Frenkel, Phys. Rev. Lett. **77**, 3149 (1996).
 - ³⁵ M. S. Diakhate, *Theory of laser-induced ultrafast structural changes in solids*, Doctoral dissertation, Universit  t Kassel (2010).
 - ³⁶ D. H. Kim, H. Ehrenreich, and E. Runge, Solid State Communications **89**, 119 (1994).
 - ³⁷ K. Zickfeld, M. E. Garcia, and K. H. Bennemann, Phys. Rev. B **59**, 13422 (1999).
 - ³⁸ N. Medvedev, V. Tkachenko, and B. Ziaja, Contributions to Plasma Physics **55**, 12 (2015).

- ³⁹ D. S. Ivanov and L. V. Zhigilei, Phys. Rev. B **68**, 064114 (2003).
- ⁴⁰ M. V. Shugaev and L. V. Zhigilei, Computational Materials Science **166**, 311 (2019).
- ⁴¹ V. Lipp and B. Ziaja, Modelling **3**, 333 (2022).
- ⁴² S. Sakong, P. Kratzer, S. Wall, A. Kalus, and M. Horn-von Hoegen, Phys. Rev. B **88**, 115419 (2013).
- ⁴³ A. Castro, M. A. L. Marques, J. A. Alonso, G. F. Bertsch, and A. Rubio, The European Physical Journal D - Atomic, Molecular, Optical and Plasma Physics **28**, 211 (2004).
- ⁴⁴ G. Wachter, *Simulation of condensed matter dynamics in strong femtosecond laser pulses*, Ph.D. thesis, Technischen Universität Wien (2014).
- ⁴⁵ A. Bende, in *Annual Reports in Computational Chemistry*, Vol. 11 (Elsevier, 2015) pp. 103–146.
- ⁴⁶ Y. Miyamoto, Scientific Reports **11**, 14626 (2021).
- ⁴⁷ C. Shepard, R. Zhou, D. C. Yost, Y. Yao, and Y. Kanai, The Journal of Chemical Physics **155**, 100901 (2021).
- ⁴⁸ M. Malinauskas, A. Žukauskas, S. Hasegawa, Y. Hayasaki, V. Mizeikis, R. Buividas, and S. Juodkazis, Light: Science & Applications **5**, e16133 (2016).
- ⁴⁹ K. Sugioka, Nanophotonics **6**, 393 (2017).
- ⁵⁰ R. Stoian and J.-P. Colombier, Nanophotonics **9**, 4665 (2020).
- ⁵¹ A. Y. Vorobyev and C. Guo, Laser & Photonics Reviews **7**, 385 (2013).
- ⁵² C.-W. Cheng and J.-K. Chen, in *Laser Ablation-From Fundamentals to Applications* (IntechOpen, 2017).
- ⁵³ L. Hong, X. Wang, H. Zheng, H. Wang, H. Yu, *et al.*, Applied Surface Science **297**, 134 (2014).
- ⁵⁴ W.-O. Siew, W.-K. Lee, H.-Y. Wong, T.-K. Yong, S.-S. Yap, and T.-Y. Tou, Applied Physics A **101**, 627 (2010).
- ⁵⁵ Q. Wang and W. Zhou, Optical Materials **72**, 508 (2017).
- ⁵⁶ B. R. Tull, J. E. Carey, E. Mazur, J. P. McDonald, and S. M. Yalisove, MRS bulletin **31**, 626 (2006).
- ⁵⁷ J. Wang, Z. Yue, H. Lu, and J. Chen, Vacuum **205**, 111417 (2022).
- ⁵⁸ A. Majid, N. Rani, M. F. Malik, N. Ahmad, F. Husain, A. Shakoor, *et al.*, Ceramics International **45**, 8069 (2019).
- ⁵⁹ D. Mazey, R. Nelson, and R. Barnes, Philosophical Magazine **17**, 1145 (1968).
- ⁶⁰ V. Schmidt, J. V. Wittemann, S. Senz, and U. Gösele, Advanced Materials **21**, 2681 (2009).
- ⁶¹ T. Moustakas, Journal of Electronic Materials **8**, 391 (1979).
- ⁶² M. Asheghi, K. Kurabayashi, R. Kasnavi, and K. Goodson, Journal of applied physics **91**, 5079 (2002).
- ⁶³ M. Lee, Nature Physics **1** (2023).
- ⁶⁴ C. Zhang, S. Chang, and Y. Dan, Advances in Physics: X **6**, 1871407 (2021).
- ⁶⁵ I. Marri, E. Degoli, and S. Ossicini, Progress in Surface Science **92**, 375 (2017).
- ⁶⁶ A. A. Istratov and E. R. Weber, Journal of The Electrochemical Society **149**, G21 (2001).
- ⁶⁷ R. Duffy, M. Shayesteh, I. Kazadojev, and R. Yu, in *2013 13th International Workshop on Junction Technology (IWJT)* (2013) pp. 16–21.
- ⁶⁸ V. Popelensky, G. Chernysheva, N. Kononov, S. Bubenov, A. Vinokurov, and S. Dorofeev, Inorganic Chemistry Communications **141**, 109602 (2022).
- ⁶⁹ Z.-Y. Zhao and P.-Z. Yang, Physical Chemistry Chemical Physics **16**, 17499 (2014).
- ⁷⁰ Y. A. Astrov, L. Portsel, A. Lodygin, V. Shuman, and E. Beregin, in *Gettering and Defect Engineering in Semiconductor Technology XI*, Solid State Phenomena, Vol. 108 (Trans Tech Publications Ltd, 2005) pp. 401–406.
- ⁷¹ Z. Fan, D. Cui, Z. Zhang, Z. Zhao, H. Chen, Y. Fan, P. Li, Z. Zhang, C. Xue, and S. Yan, Nanomaterials **11**, 41 (2021).
- ⁷² J. Lv, T. Zhang, P. Zhang, Y. Zhao, and S. Li, Nanoscale research letters **13**, 1 (2018).
- ⁷³ Q. Tan, F. Lu, C. Xue, W. Zhang, L. Lin, and J. Xiong, Sensors and Actuators A: Physical **295**, 560 (2019).
- ⁷⁴ M. Otto, M. Algasinger, H. Branz, B. Gesemann, T. Gimpel, K. Fücksel, T. Käsebier, S. Kontermann, S. Koynov, X. Li, *et al.*, Advanced optical materials **3**, 147 (2015).
- ⁷⁵ X. Liu, P. R. Coxon, M. Peters, B. Hoex, J. M. Cole, and D. J. Fray, Energy & Environmental Science **7**, 3223 (2014).
- ⁷⁶ M. Casalino, G. Coppola, M. Iodice, I. Rendina, and L. Sirleto, Sensors **10**, 10571 (2010).
- ⁷⁷ M. A. Juntunen, J. Heinonen, V. Vähänissi, P. Repo, D. Valluru, and H. Savin, Nature Photonics **10**, 777 (2016).
- ⁷⁸ X. Li, Z. Gao, D. Zhang, K. Tao, R. Jia, S. Jiang, B. Wang, Z. Ji, Z. Jin, and X. Liu, Solar Energy **195**, 176 (2020).
- ⁷⁹ E. Özkol, P. Procel, Y. Zhao, L. Mazzarella, R. Medlin, P. Šutta, O. Isabella, and M. Zeman, physica status solidi (RRL)—Rapid Research Letters **14**, 1900087 (2020).
- ⁸⁰ M. Abdullah, M. Alghoul, H. Naser, N. Asim, S. Ahmadi, B. Yatim, and K. Sopian, Renewable and Sustainable Energy Reviews **66**, 380 (2016).
- ⁸¹ L.-H. Liu, S.-H. Cui, T.-Z. Fu, Y. Yuan, and C.-B. Li, Applied Surface Science **464**, 337 (2019).
- ⁸² X.-L. Liu, S.-W. Zhu, H.-B. Sun, Y. Hu, S.-X. Ma, X.-J. Ning, L. Zhao, and J. Zhuang, ACS applied materials & interfaces **10**, 5061 (2018).
- ⁸³ A. E. Lim, C. Y. Lim, Y. C. Lam, and R. Taboryski, Micromachines **9**, 229 (2018).
- ⁸⁴ K.-M. Guenther, T. Gimpel, S. Kontermann, and W. Schade, Applied Physics Letters **102** (2013).
- ⁸⁵ P. Mc Kearney, I. Lebershausen, S. Schäfer, S. Paulus, and S. Kontermann, Journal of Laser Micro/Nanoengineering **18**, 72 (2023).
- ⁸⁶ N. Pirouzfam, k. sendur, and A. Keçebaş, Journal of Applied Physics **129** (2021), 10.1063/5.0047153.
- ⁸⁷ P. Mc Kearney, S. Schäfer, S. Paulus, M. Roser, F. Piermaier, I. Lebershausen, and S. R. Kontermann, Journal of Applied Physics **133** (2023).
- ⁸⁸ C.-H. Hsu, J.-R. Wu, Y.-T. Lu, D. J. Flood, A. R. Barron, and L.-C. Chen, Materials Science in Semiconductor Processing **25**, 2 (2014), special topical issue on Materials for Green Energy and the Environment.
- ⁸⁹ H. Savin, P. Repo, G. von Gastrow, P. Ortega, E. Calle, M. Garín, and R. Alcubilla, Nature Nanotechnology **10**, 624 (2015).
- ⁹⁰ C. H. Crouch, J. E. Carey, M. Shen, E. Mazur, and F. Y. Génin, Applied Physics A **79**, 1635 (2004).
- ⁹¹ Y. Wang, Y. P. Liu, H. L. Liang, Z. X. Mei, and X. L. Du, Phys. Chem. Chem. Phys. **15**, 2345 (2013).
- ⁹² T. Sarnet, M. Halbwax, R. Torres, P. Delaporte, M. Sentis, S. Martinuzzi, V. Vervisch, F. Torregrosa, H. Etienne, L. Roux, *et al.*, in *Commercial and Biomedical Applica-*

- tions of Ultrafast Lasers VIII*, Vol. 6881 (International Society for Optics and Photonics, 2008) p. 688119.
- ⁹³ J. Müllerová, L. Scholtz, J. Ďurišová, E. Pinčík, M. Solanská, and D. Pudiš, *Applied Surface Science* **461**, 182 (2018).
- ⁹⁴ X. Zhang, S. Collins, and R. Smith, *Journal of the electrochemical society* **136**, 1561 (1989).
- ⁹⁵ H. Mei, C. Wang, J. Yao, Y.-C. Chang, J. Cheng, Y. Zhu, S. Yin, and C. Luo, *Optics Communications* **284**, 1072 (2011).
- ⁹⁶ E. S. Zijlstra, A. Kalitsov, T. Zier, and M. E. Garcia, *Advanced Materials* **25**, 5605 (2013).
- ⁹⁷ T. Zier, E. S. Zijlstra, S. Krylow, and M. E. Garcia, *Applied Physics A* **123**, 1 (2017).
- ⁹⁸ S. Goedecker, M. Teter, and J. Hutter, *Phys. Rev. B* **54**, 1703 (1996).
- ⁹⁹ E. Prince, *International Tables for Crystallography, Volume C: Mathematical, physical and chemical tables* (Springer Science & Business Media, 2004) p. 556.
- ¹⁰⁰ T. Zier, E. S. Zijlstra, and M. E. Garcia, *Applied Physics A* **117**, 1 (2014).